

## Article

# Insights into the Mechanism, Regio-/Diastereoselectivities and Ligand Role of Nickel-Initiated [3+2] Cycloadditions between Vinylcyclopropane and *N*-Tosylbenzaldimine

Weihua Mu <sup>\*</sup>, Lin Zhu, Shuya Xia, Xue Tan, Liangfei Duan, Guanghao Meng and Guo Liu <sup>\*</sup>

Faculty of Chemistry and Chemical Engineering, Yunnan Normal University, Kunming 650092, China; zl000270@163.com (L.Z.); xiashuya@126.com (S.X.); tx000502@163.com (X.T.); liangfeiduan1012@163.com (L.D.); mengguanghao@ynnu.edu.cn (G.M.)

<sup>\*</sup> Correspondence: weihua\_mu@ynnu.edu.cn (W.M.); liuguo@ynnu.edu.cn (G.L.)

**Abstract:** Density functional theory (DFT) was employed to explore the reaction mechanism, regio- and diastereoselectivities of nickel-initiated [3+2] cycloaddition between vinylcyclopropane (VCP) and *N*-tosylbenzaldimine assisted by phosphine ligands. Four different binding modes of the nickel center to VCP substrate were explored during the ring-opening of VCP, among which the *C,C\_anti* and *C,C\_syn* modes were verified to be the most accessible ones. Further explorations about four different phosphine ligand-assisted reactions based on the two most probable binding modes show that the difference in binding mode of bi- and monodentate phosphine ligands can vary the optimal reaction pathway, especially in the [3+2] cycloaddition process between the ring-opened intermediate and *N*-tosylbenzaldimine. The formation of C–C and C–N bonds between *N*-tosylbenzaldimine and the ring-opened intermediate through [3+2] cycloaddition is found to be stepwise, with the former acting as the rate-determining step (RDS) in most cases. Computed free energy barriers of RDS transition states on the optimal path I or II not only give out good predictions for reaction rates and half-lives, but also provide reasonable explanations for the major generation of *cis*-pyrrolidine. Noncovalent interaction analyses of key stationary points suggest the rate is influenced by both electronic effects and steric hindrance, while the diastereoselectivity is mainly controlled by electronic effects.

**Keywords:** nickel; catalysis; vinylcyclopropane (VCP); [3+2] cycloaddition; mechanism; DFT; diastereoselectivity



**Citation:** Mu, W.; Zhu, L.; Xia, S.; Tan, X.; Duan, L.; Meng, G.; Liu, G. Insights into the Mechanism, Regio-/Diastereoselectivities and Ligand Role of Nickel-Initiated [3+2] Cycloadditions between Vinylcyclopropane and *N*-Tosylbenzaldimine. *Catalysts* **2024**, *14*, 82. <https://doi.org/10.3390/catal14010082>

Academic Editor: Francisco J. Fernández-Alvarez

Received: 31 December 2023

Revised: 14 January 2024

Accepted: 16 January 2024

Published: 18 January 2024



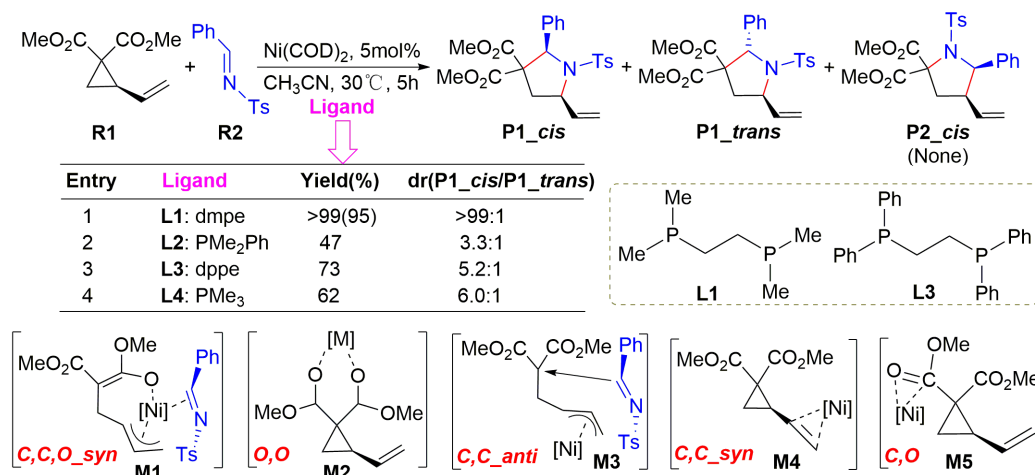
**Copyright:** © 2024 by the authors. Licensee MDPI, Basel, Switzerland. This article is an open access article distributed under the terms and conditions of the Creative Commons Attribution (CC BY) license (<https://creativecommons.org/licenses/by/4.0/>).

## 1. Introduction

Heterocycles such as pyrrolidines are important backbones in organic chemistry and widely distributed in bioactive molecules and natural products [1–4]. For decades, significant efforts have been made to its stereoselective synthesis, among which transition metal-catalyzed cycloaddition has been established as a powerful tool for its atomic economy and facilities in multi-bond formation in a single step [5–12]. Benefitting from nickel's wide distribution and availability, as well as the excellent performance of phosphine ligands in controlling selectivities [13–17], nickel-mediated multi-component cycloadditions assisted by phosphine ligands have emerged as a facile strategy for constructing pyrrolidine derivatives for years [18,19].

In 2015, Matsubara and co-workers developed a nickel-catalyzed intermolecular [3+2] cycloaddition of vinylcyclopropanes (**R1**) to *N*-tosylbenzaldimine (**R2**), and obtained substituted pyrrolidines in high yields with good regio- and diastereoselectivities (Scheme 1) [20]. This reaction can proceed under mild conditions, has good tolerance for a variety of imines and led to overwhelming formation of *cis*-pyrrolidines (**P1\_cis**). Moreover, when the bidentate dmpe ligand was replaced by monodentated  $\text{PMe}_2\text{Ph}$ , both the yield and diastereoselectivity ratio (dr, **P1\_cis**:**P1\_trans**) dropped dramatically. This indicates the phosphine ligands should have played an important role in controlling the rate and selectivity of

this reaction. To the best of our knowledge, few studies have made explanations for the strong effect of phosphine ligands on the rates and selectivities in this or other similar Ni-catalyzed multi-component cycloadditions involving vinylcyclopropanes and imines, albeit a number of works have demonstrated the importance of ligand effects on other types of reactions theoretically [21–25].



**Scheme 1.** Nickel-mediated intermolecular [3+2] cycloaddition of vinylcyclopropanes (VCP) to imines assisted by phosphine ligands [20], with literature-speculated intermediates (M1–M5) depicted as well.

Based on the literature report about the Pd(0)-catalyzed ring-opening of vinylcyclopropanes with aldehydes [26], Matsubara proposed a heteronickelacycle intermediate **M1** (in which Ni atom coordinates in *C,C,O<sub>syn</sub>* mode, Scheme 1) would be formed before the pyrrolidines were finally produced through a nucleophilic attack of vinylcyclopropanes on *N*-tosylbenzaldimine. Interestingly, some Lewis acid (LA)-catalyzed ring-openings of vinylcyclopropanes or epoxyethane show an alternative binding mode of LA onto the two oxygen atoms in  $-\text{CO}_2\text{Me}$  groups of vinylcyclopropane substrates (**M2**, *O,O* binding mode) both experimentally and computationally [27–32]. Still, a few other transition metal-catalyzed reactions show a coordination model similar to **M3** (*C,C<sub>anti</sub>* mode) in Scheme 1 [33,34]. Considering the differences of coordinates in bidentate and monodentate phosphine ligands such as dmpe and  $\text{PMe}_2\text{Ph}$ , the *C,C<sub>syn</sub>* mode (**M4**) is also possible. Moreover, a *C,O* mode (**M5**) would emerge when the nickel center coordinates with the  $\text{C}=\text{O}$  double bond in one of the  $-\text{CO}_2\text{Me}$  groups of **R1**. However, due to the lack of comprehensive explorations at a molecular level, the following issues, such as (1) which mode is the most accessible one, (2) whether the heteronickelacycle intermediate **M1** locates on the optimal reaction pathway, and (3) what is the role of phosphine ligand in this reaction, still remain unclear.

To explore the reaction mechanism, the origin of regio- and diastereoselectivities, as well as the role of phosphine ligands in controlling rates and diastereoselectivities, we have conducted comprehensive computational studies on the nickel-initiated [3+2] cycloaddition between vinylcyclopropane and *N*-tosylbenzaldimine. Detailed microscopic mechanisms leading to the formation of *cis*-pyrrolidines (**P1<sub>cis</sub>**) are characterized, with the *C,C<sub>anti</sub>* (**M3**) and *C,C<sub>syn</sub>* (**M4**) modes being confirmed as the most accessible ones when bi- and monodentate phosphine ligands are employed, respectively (Scheme 1). In addition, the regioselectivities and four different phosphine ligand-assisted diastereoselectivities are also computed and discussed in depth.

## 2. Results and Discussion

### 2.1. Mechanism

To explore the possible binding modes of phosphine ligand to the nickel center in the nickel-initiated [3+2] cycloaddition between vinylcyclopropanes (VCP, **R1**) and *N*-tosylbenzaldimine (**R2**), we have conducted calculations at the IDSCRF(ACN)-B3LYP/DGDZVP level in acetonitrile (ACN) solvent firstly, to see if the active Ni(COD)L species can be generated in situ from the precatalyst Ni(COD)<sub>2</sub> and phosphine ligands (**L1**–**L4**). As shown in Figure 1, the formation of Ni(COD)L is exothermic and releases about 6.9–16.2 kcal·mol<sup>-1</sup> of free energy, indicating a facile formation of Ni(COD)L species under the corresponding experimental temperature (303 K). Thus, Ni(COD)L is taken as the initial catalyst throughout the work and all potential free energy surfaces (PESs) are adjusted to the starting points of Ni(COD)L+**R1** accordingly.

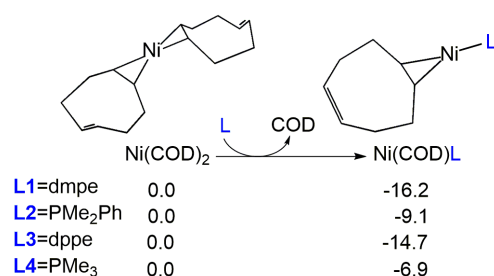


**Figure 1.** Energetics ( $\Delta G$ , in kcal·mol<sup>-1</sup>) during the in situ generation of Ni(COD)L species from Ni(COD)<sub>2</sub> and different phosphine ligands (**L1**–**L4**).

#### 2.1.1. The Ring-Opening of VCP

Upon the formation of Ni(COD)L species, three possible reaction channels (paths **I**–**III** correspond to *C,C*<sub>anti</sub>, *C,C*<sub>syn</sub> and *O,O* binding modes, respectively) for C(1)–C(3) bond cleavage in **R1** were located (Figure 2). On *C,C*<sub>anti</sub> path **I**, the Ni-dmpe (**L1**) center interacts with the vinyl group from the *anti* side of the two –CO<sub>2</sub>Me groups so as to avoid possible steric hindrance arising between them, bearing only a 1.0 kcal·mol<sup>-1</sup> activation free energy barrier when the ring-opened intermediate **INT1\_I** is formed. Due to possible steric hindrance arising between one of the two –CO<sub>2</sub>Me groups in **R1** and the –Me group in the dmpe fragment, *C,C*<sub>syn</sub> path **II** bears an activation barrier of 7.0 kcal·mol<sup>-1</sup>, about 6.0 kcal·mol<sup>-1</sup> higher than that of **TS1\_I** on path **I**. Although **TS1\_II** can also be overcome at a temperature of 303 K, an activation barrier as high as seven times that corresponding to **TS1\_I** would shrink path **II**'s contribution to some degree. Similar to Tomilov's speculation in the LA-catalyzed ring-opening of VCP [27], an *O,O* binding path **III** in which the Ni-dmpe center coordinates with the two carbonyl oxygen atoms in the –CO<sub>2</sub>Me groups of **R1** can also be located. However, corresponding stationary points (**COM1\_III**, **TS1\_III** and **INT1\_III**) are extraordinarily more unstable than their alternatives on paths **I** and **II**, suggesting little possibility for **R1** to break the C(1)–C(3) bond through path **III**, as shown in Figures 2 and S1.

Inspired by Zhang's report about epoxyethane derivative's ring-opening through O2–C3 bond cleavage [29] and Wang's work about VCP's ring-opening through C(2)–C(3) bond cleavage [35], we continued to explore the possible regioselective ring-opening of **R1** through C(1)–C(2) (path **IV**) and C(2)–C(3) (path **V**) bonds cleavage. Given Ni-dmpe coordinated with one of the C=O double bonds in the –CO<sub>2</sub>Me groups, a complex **COM1\_IV** based on the *C,O* coordination mode could be located, being endothermic of 11.3 kcal·mol<sup>-1</sup> of free energies. As shown in Figure 2, the activation free energy barrier of **TS1\_IV** corresponding to C(1)–C(2)'s cleavage is so high, 22.8 kcal·mol<sup>-1</sup>, that path **IV** has little competitiveness when compared with paths **I** and **II**. Similarly, the extremely high activation barrier of **TS1\_V** (27.6 kcal·mol<sup>-1</sup>) should block off the possibility of C(2)–C(3)'s cleavage through path **V** (derived from *C,C*<sub>anti</sub> mode) totally. The extraordinary higher activation barriers of **TS1\_IV** and **TS1\_V** (corresponding to C(1)–C(2) and C(2)–C(3)'s

cleavage, respectively) provide good explanations for the disappearance of any regioisomer in experiments [20].

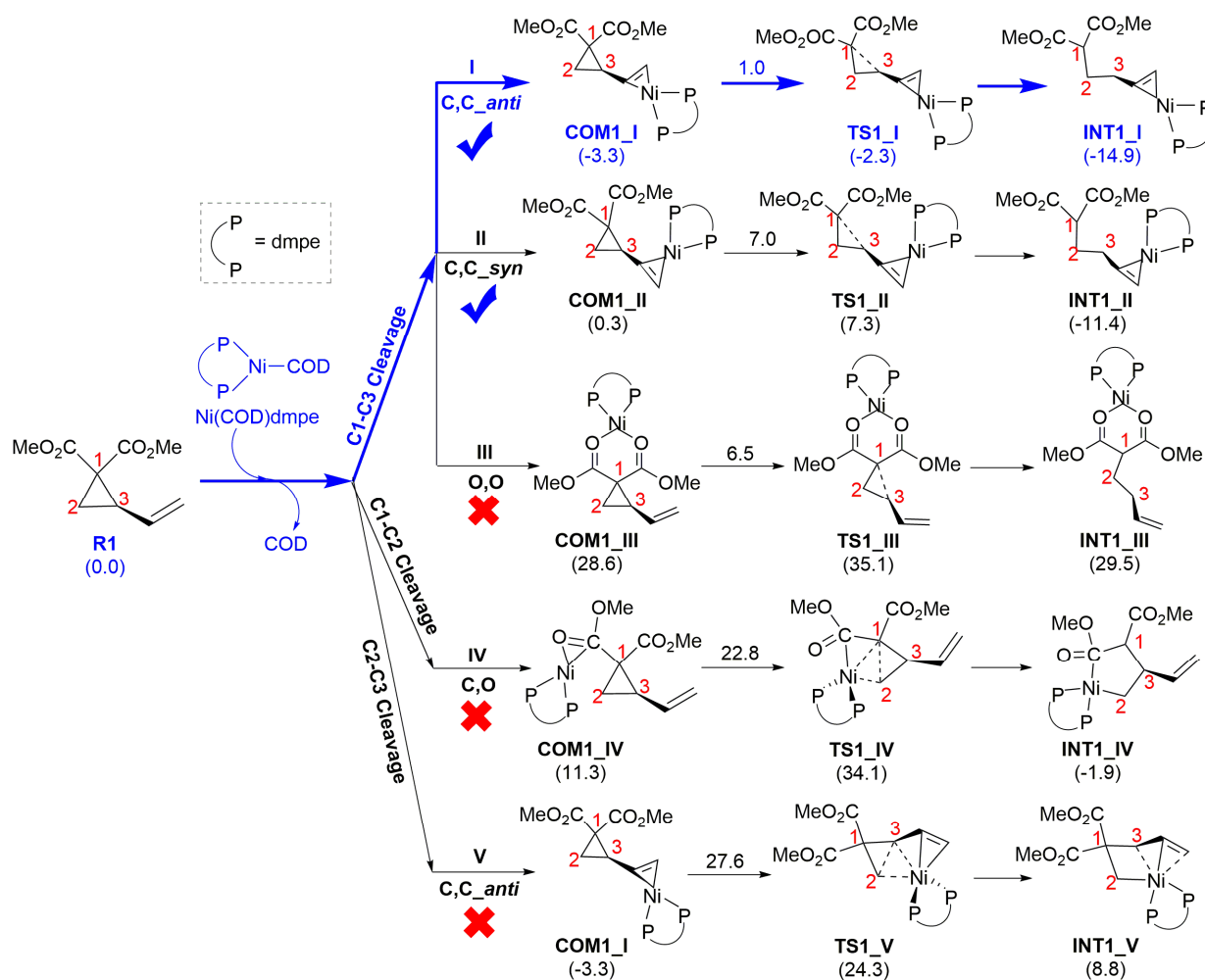


**Figure 2.** Possible reaction mechanism and energetics ( $\Delta G$ , in kcal·mol<sup>-1</sup>) for the ring-opening of vinylcyclopropane (VCP).

Endeavors had also been made to locate a C<sub>1</sub>C<sub>3</sub>O<sub>syn</sub> binding complex COM1\_V (similar to M1 in Scheme 1), which was speculated based on experiments, but all location failed (Figure S2). It seems a four-coordinated nickel center is saturated already and has no extra coordinate for the oxygen atom in the -CO<sub>2</sub>Me group. Namely, path I, featuring a C<sub>1</sub>C<sub>3</sub> anti binding mode, presents the most accessible pathway of VCP's ring-opening, while path II, corresponding to the C<sub>1</sub>C<sub>3</sub> syn binding mode, is also surmountable. The formation of intermediate INT1\_I only needs to overcome a free energy barrier of 1.0 kcal·mol<sup>-1</sup> and is exothermic by a free energy of 14.9 kcal·mol<sup>-1</sup>, and thus very facile under the experimental temperature (303 K). The formation of INT1\_II is a little more difficult but also exothermic and practicable.

Optimized structures of stationary points located on paths I–V, accompanied by key geometrical parameters and necessary Wiberg bond indices (WBI) derived from natural bond orbital (NBO) analysis [36–38], are presented in Figure 3 and Figure S3, respectively. It is interesting that most stationary points featuring  $\eta^4$ -coordinate and planar configuration of the nickel center are stable, while others which feature  $\eta^5$ - or  $\eta^6$ -coordinated (TS1\_IV and TS1\_V) and non-planar  $\eta^4$ -coordinated nickel centers (TS1\_III and COM1\_III) are relatively unstable. This fascinating dependence of relative energies on coordinate and coordination mode, similar to Scott's finding in the Cr(II) Phillips ethylene polymerization

catalyst [39], urged us to conduct further QTAIM [40,41] topological analyses about selected stationary points, with corresponding results presented in Figure S4.

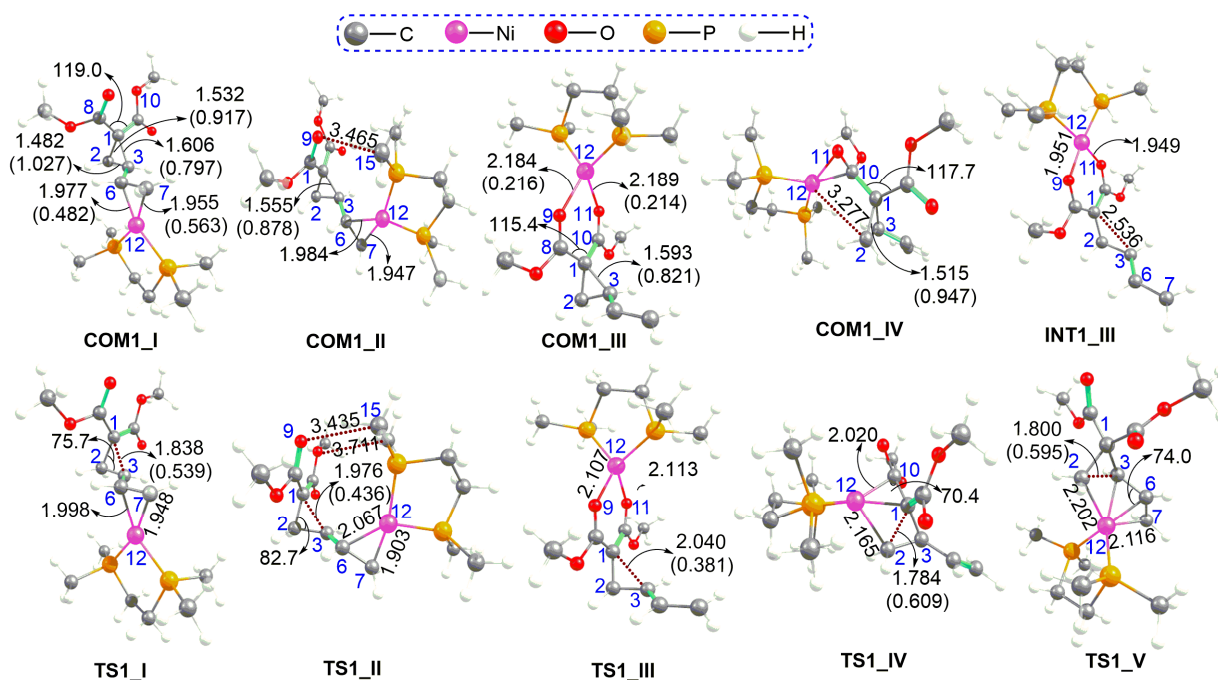


**Figure 3.** Optimized geometries (with bond length in Å and angle in °) of key stationary points located on paths I–V, accompanied by necessary Wiberg bond indices (WBI).

The  $\eta^4$ -,  $\eta^5$ - or  $\eta^6$ -coordinates of the nickel center in all stationary points on paths I–V were confirmed by four, five or six bond critical points (BCPs) around the nickel center, respectively, with BCPs electron densities of Ni–X (X=C,O,P) bonds being 0.0471–0.1198  $\text{e}\cdot\text{bohr}^{-3}$  (Figure S4). According to the QTAIM analysis results, the relative instability of non-planar  $\eta^4$ -coordinated **TS1\_III** and **COM1\_III**, as well as  $\eta^5$ - or  $\eta^6$ -coordinated **TS1\_IV** (or **TS1\_V**), is probably caused by a distortion of their geometries from the stable square planar  $\eta^4$ -coordinated conformation. The unexpected higher free energies of planar  $\eta^4$ -coordinated **INT1\_III** could be attributed to a deviation of several bond angles in it from that in reactant **R1** ( $-7.1$ – $+4.6^\circ$ , Figure S5), for the distortion effect has already been identified to be essential in elevating the structure’s instabilities [42–45]. The relative higher free energies and activation barrier of **TS1\_II** over **TS1\_I** should arise from steric hindrance between  $-\text{Me}$  and  $-\text{CO}_2\text{Me}$  groups in the former, as identified by shorter C–H...O distances (3.435–3.711 Å) and four extra BCPs between them (with electron densities at  $-0.0049$ – $0.0093$   $\text{e}\cdot\text{bohr}^{-3}$ , Figure S4). Weaker complexation between Ni, P and O atoms in **COM1\_III** than that between Ni, P and vinyl–C atoms in **COM1\_I** also contributes to the former’s instability, as verified by the smaller electron densities of these four BCPs in **COM1\_III** than in **COM1\_I**.

Natural population analysis (NPA) results for key stationary points on paths I–V also support the regioselective ring-opening of **R1** well. For example, the WBIs for C(1)–C(3), C(1)–C(2) and C(2)–C(3) in **COM1\_I** are 0.797, 0.917 and 1.027, respectively (Figure 3), indicating the weakest bondage between C(1) and C(3) atoms and the easiest cleavage of it, in good agreement with previous energetic results. In addition, the difference of WBI values corresponding to the breaking C(1)–C(3) bond in **COM1\_I** and **TS1\_I** is  $-0.258$ , smaller than all counterparts on paths II–V (C(1)–C(3) on paths II–III, C(1)–C(2) on path IV and C(2)–C(3) on path V, respectively), which evidences the easiest cleavage of the C(1)–C(3) bond in **R1** (through  $C,C_{anti}$  path I) well and rationalizes the smooth formation of intermediate **INT1\_I**.

### 2.1.2. The [3+2] Cycloaddition of INT1 with *N*-Tosylbenzaldimine

After confirmation of *C,C\_anti* path I as the dominant pathway in generating intermediate **INT1\_I** through C(1)–C(3) cleavage of **R1** (Figure 2), we continued to explore if the *C,C\_anti* path is still dominant in the subsequent [3+2] cycloaddition process of intermediate **INT1** with *N*-tosylbenzaldimine. Since paths IV and V, which correspond to C(1)–C(2) and C(2)–C(3) bonds cleavage of **R1**, are precluded by extremely high activation barriers of **TS1\_IV** and **TS1\_V** (Figure 2 and Figure S1), only the *C,C\_anti*, *C,C\_syn* and *O,O* binding modes (paths I–III) were explored in Section 2.1.2, with the most probable paths **Ia\_cis** and **Iia\_cis** presented in Figures 4 and 5, respectively.

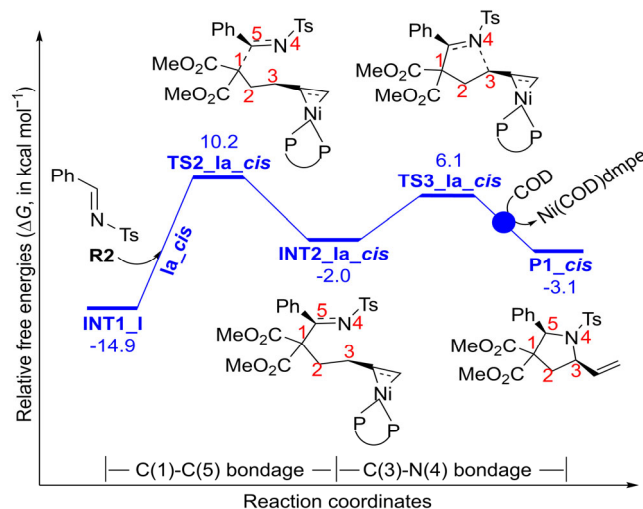


**Figure 4.** Potential free energy surfaces (PESs) for path **Ia\_cis**.

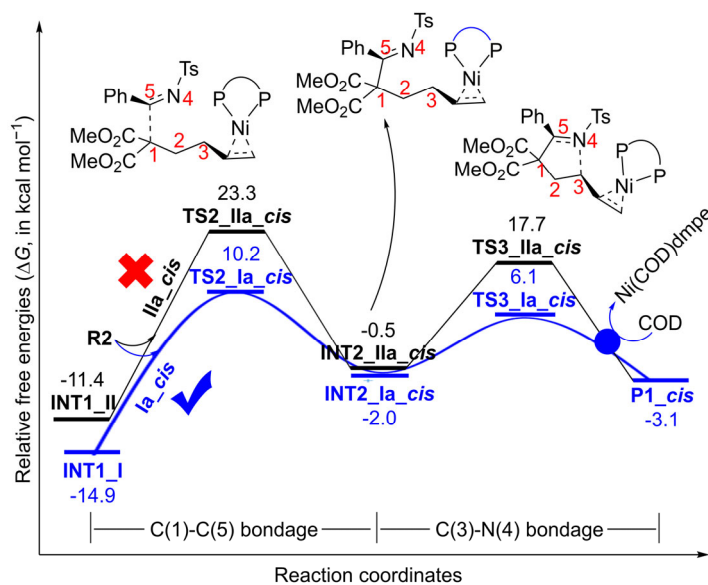


**Figure 5.** Potential free energy surfaces (PESs) for path **Iia\_cis** (black), with that for path **Ia\_cis** (blue) plotted for the convenience of comparison.

On *C,C\_anti* path I, the C(5) atom in *N*-tosylbenzaldimine (**R2**) attacks the C(1) atom in **INT1\_I** firstly, overcomes an activation barrier of 25.1 kcal·mol<sup>-1</sup> (**TS2\_Ia\_cis**) and leads to the formation of intermediate **INT2\_Ia\_cis** (Figure 4). Then the N(4) atom in **INT2\_Ia\_cis** bonds with the C(3) atom through **TS3\_Ia\_cis**, overcoming an activation barrier of 8.1 kcal·mol<sup>-1</sup> and transforming itself into the *cis*-pyrrolidine product (**P1\_cis**) smoothly. As the activation barrier of **TS3\_Ia\_cis** (8.1 kcal·mol<sup>-1</sup>) is much lower than that of **TS2\_Ia\_cis** (25.1 kcal·mol<sup>-1</sup>), and **TS3\_Ia\_cis** is apparently more stable than **TS2\_Ia\_cis**,

the bonding between C(1) and C(5) atoms (through **TS2\_Ia\_cis**) acts as the rate-determining step (RDS) of the whole reaction. Finally, the re-involving of the COD ligand helps to recycle Ni(COD)L1 species accompanying **P1\_cis**'s production.

The formation of **INT1\_II** through *C,C\_syn* path **II** has also been verified to be practicable during the VCP's ring-opening process (Figure 2), so massive efforts were made to see if its subsequent process is still accessible. The stepwise mechanism and RDS characteristic on *C,C\_syn* path **II** are similar to the *C,C\_anti* path **I**. However, the whole PESs of the *C,C\_syn* path **II** are above that of *C,C\_anti* path **I**, and the RDS step's activation barrier on path **II** is as high as  $34.7 \text{ kcal}\cdot\text{mol}^{-1}$  (**TS2\_IIa\_cis**, Figure 5), about  $9.6 \text{ kcal}\cdot\text{mol}^{-1}$  higher than that of **TS2\_Ia\_cis**. Moreover, the activation barrier of **TS3\_IIa\_cis** is elevated to be  $18.2 \text{ kcal}\cdot\text{mol}^{-1}$ , more than twice that of **TS3\_Ia\_cis** ( $8.1 \text{ kcal}\cdot\text{mol}^{-1}$ ). These energetic results illustrate *C,C\_anti* path **I** has absolute priority in directing the formation of **P1\_cis** when the bidentate phosphine ligand **dmpe** (**L1**) is employed.

Further explorations about *O,O* binding path **III** locate even higher potential energy surfaces than *C,C\_syn* path **II** (Figure S6), and the whole PESs lay much higher above the starting materials (**R1**+Ni(COD)L1, Figure 2). Although the computed PESs for *O,O* binding path **III** are comparable with previously reported Sn(OTf)<sub>2</sub>-catalyzed C–O cleavage of epoxyethane [29], the difficulty in generating **INT1\_III** plus the extraordinarily higher-located PESs of *O,O* binding path **III** leave no possibility for this reaction to proceed along it according to the lowest-energy principle framed in transition state theory [46]. Other mechanistic possibilities such as C(3)–N(4)'s bonding prior to C(1)–C(5) on *C,C\_anti* path **I** (path **Ib\_cis**) and *C,C\_syn* path **II** (path **IIB\_cis**), as well as C(1)–C(5)'s bonding prior to C(3)–N(4) on *O,O* binding path **III** (path **IIIa\_cis**) were also checked, with corresponding results summarized in Figure S7. The activation barriers corresponding to **TS2\_Ib\_cis** and **TS2\_IIB\_cis** are predicted to be  $51.5$  and  $51.8 \text{ kcal}\cdot\text{mol}^{-1}$ , respectively, both too high to be overcome under the given experimental temperature (303 K). Similarly, reaction along *O,O* binding path **IIIa\_cis**, in which the C(1)–C(5) bonding occurs, is blocked off totally by the higher activation barrier of **TS2\_IIIa\_cis** than **TS2\_Ia\_cis** ( $29.0$  versus  $25.1 \text{ kcal}\cdot\text{mol}^{-1}$ ), as well as by the extraordinarily higher relative energies of **TS2\_IIIa\_cis** than **TS2\_Ia\_cis** ( $58.5$  versus  $10.2 \text{ kcal}\cdot\text{mol}^{-1}$ ).

As shown in Figure 6, a smaller cavity volume and surface of **TS2\_IIa\_cis** ( $1042.5 \text{ \AA}^3$  and  $709.5 \text{ \AA}^2$ , respectively) than that of **TS2\_Ia\_cis** ( $1056.3 \text{ \AA}^3$  and  $746.9 \text{ \AA}^2$ , respectively) indicates the more compacted geometry of the former. Thereby, the relative instability of **TS2\_IIa\_cis** to **TS2\_Ia\_cis** is attributed to the greater spatial hinderance arising in it between the nickel center and the carbon chain in the ring-opened **INT1\_I** fragment. Noncovalent interaction (NCI) [47] analysis about **TS2\_Ia\_cis** and **TS2\_IIa\_cis** shows more serious spatial repulsion (in red) and weaker noncovalent interaction (in green) in **TS2\_IIa\_cis** than in **TS2\_Ia\_cis**, and thus rationalizes the former's relative instability and higher activation barrier.

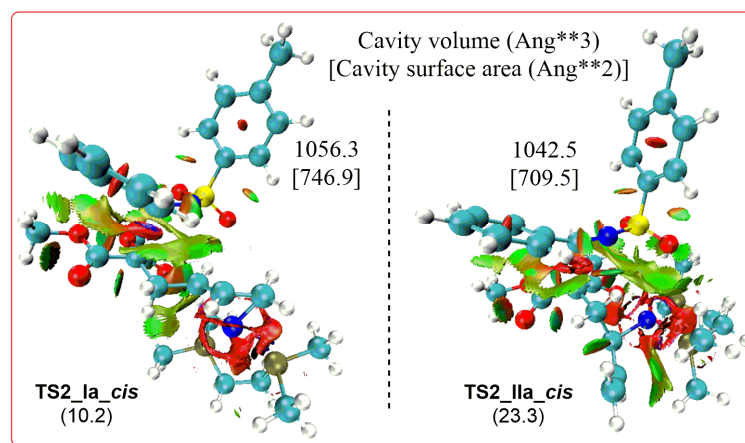


**Figure 6.** NCI analysis results for transition states **TS2\_Ia\_cis** and **TS2\_IIa\_cis**, with their cavity volumes (in  $\text{\AA}^3$ ) and surfaces (in  $\text{\AA}^2$ ) depicted.

## 2.2. Selectivities

### 2.2.1. Regioselectivities

Explorations about the alternative **P2<sub>cis</sub>** regioisomer's formation through C(1)–N(4) bonding explains well its nondetectability by an activation barrier of **TS2<sub>Ic<sub>cis</sub></sub>** being as high as 56.0 kcal·mol<sup>−1</sup> (Figure 7), in good accordance with both Matsubara's [20] and Dieskau's [48] experimental results. Further NPA charge population results show there are −0.372, −0.225, −0.735 and +0.185 charges distributed on C(1), C(3), N(4) and C(5) atoms in **INT1<sub>I</sub>** and **R2**, respectively (Table 1). That is, when the intermediate **INT1<sub>I</sub>** reacts with substrate **R2**, the more negative C(1) atom in **INT1<sub>I</sub>** prefers to attack the more positive C(5) atom in **R2**, which supports well the prior bonding of C(1)–C(5) to C(3)–N(4). NCI analysis about **TS2<sub>Ic<sub>cis</sub></sub>** shows obvious steric repulsion around the nickel center in it, and weaker noncovalent interactions than that displayed in **TS2<sub>Ia<sub>cis</sub></sub>**. Thus, **TS2<sub>Ic<sub>cis</sub></sub>** is much less stable than **TS2<sub>Ia<sub>cis</sub></sub>**, and no **P2<sub>cis</sub>** regioisomer could be detected in experiments.

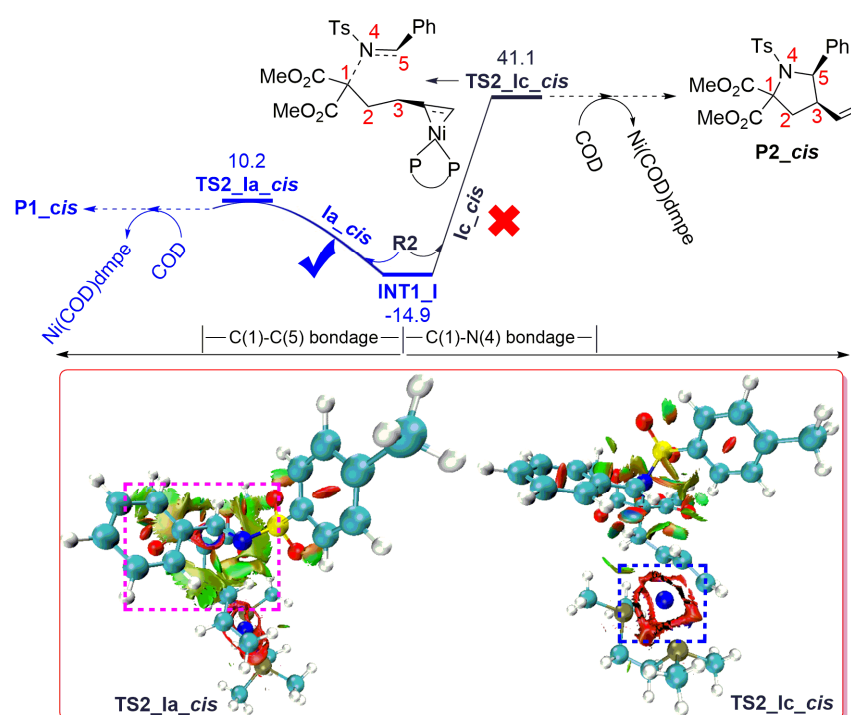


**Figure 7.** Potential free energy surfaces (PESs,  $\Delta G$  in kcal·mol<sup>−1</sup>) for path **Ic<sub>cis</sub>** (black), with the NCI analysis results of transition states **TS2<sub>Ia<sub>cis</sub></sub>** and **TS2<sub>Ic<sub>cis</sub></sub>** depicted.

**Table 1.** NPA charge population (unit:  $e^-$ ) of key atoms in reactant **R2** and intermediate **INT1<sub>I</sub>**.

	C(1)	C(3)	N(4)	C(5)
	−0.372	−0.225	−0.735	+0.185

### 2.2.2. Diastereoselectivities

Based on the aforementioned investigations on the reaction mechanism and regioselectivities, path **Ia<sub>cis</sub>** has been confirmed as the optimal reaction pathway leading to the formation of product **P1<sub>cis</sub>** in the bidentate dmpe ligand-assisted case, with the C(1)–C(5) bonding process (through **TS2<sub>Ia<sub>cis</sub></sub>**) acting as the RDS of the whole reaction. To investi-



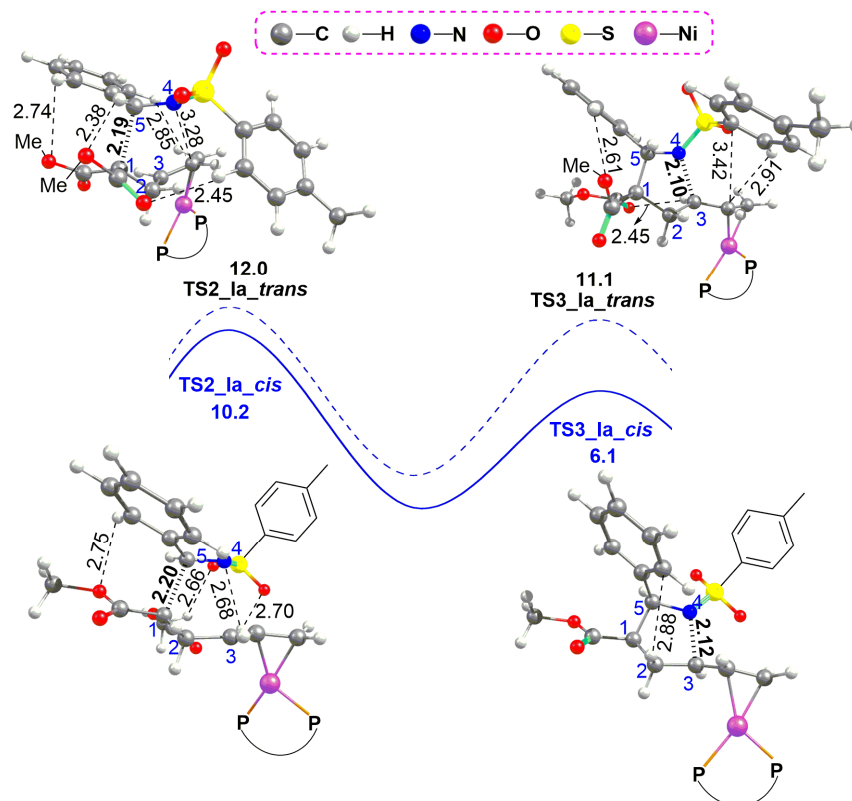
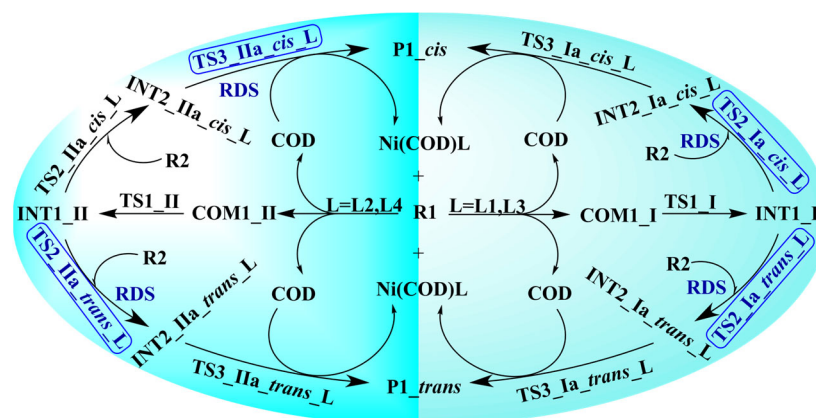


**Figure 9.** Optimized geometries (with bond length in Å) for transition states **TS2\_Ia\_cis/trans** and **TS3\_Ia\_cis/trans**.

### 2.3. Ligand Role

Matsubara and co-workers found the yield of **P1\_cis** varied a lot when different phosphine ligands were employed in their experiments (Scheme 1). For example, when the bidentate ligand **L1** (dmpe) was replaced by the monodentate ligand **L2** ( $\text{PMe}_2\text{Ph}$ ), the reaction yield decreased from >99% to 47%; when the bidentate ligand **L3** (dppe) was employed, the yield rose to 73%; the reaction yield reduced to 62% while replacing **L3** with the monodentate ligand **L4** ( $\text{PMe}_3$ ). Moreover, the ratio of **P1\_cis**:**P1\_trans** changed significantly, ranging from >99:1 to 3.3:1 when different phosphine ligands were used. These fantastic results motivated us to conduct calculations on ligand **L2**, **L3** and **L4**-assisted reactions further at the same computational level, to explore the nature and influence of phosphine ligands on the yields and selectivities of the reaction.

Computed mechanism and energy results for the aforementioned paths **Ia\_cis** and **Ia\_trans** assisted by monodentate **L2** (denoted **Ia\_cis\_L2** and **Ia\_trans\_L2**, respectively) are shown in Scheme 2 and Figure S10, respectively. The monodentate **L2**-assisted reaction also needs to go through the ring-opening of VCP and subsequent stepwise [3+2] cycloaddition sequentially, similar to the bidentate **L1**-assisted one. However, the RDS step on paths **Ia\_cis\_L2** and **Ia\_trans\_L2** corresponds no longer to the C(1)–C(5) bonding (**TS2\_Ia\_cis/trans\_L2**); instead, it corresponds to their subsequent C(3)–N(4) bonding process (**TS3\_Ia\_cis/trans\_L2**). Furthermore, the total free energy barriers of **TS3\_Ia\_cis\_L2** and **TS3\_Ia\_trans\_L2** are 40.8 and 41.9  $\text{kcal}\cdot\text{mol}^{-1}$ , respectively (Figure S10). Such high activation barriers are too difficult to be overcome at an experimental temperature of 303 K, and are inconsistent with a 47% yield of **P1** in experiments (Scheme 1).



**Scheme 2.** Probable reaction mechanism for the mono- and bidentate phosphine ligand-assisted nickel-initiated [3+2] cycloaddition between VCP and *N*-tosylbenzalimine.

The above contradiction made us speculate if the monodentate ligand **L2**-assisted paths **Ia\_cis\_L2** and **Ia\_trans\_L2** are still the optimal pathways. Thereby, calculations were conducted further on **L2**-assisted path **II**, which is also practicable in the VCP's ring-opening process (Figure 2), with results shown in Figure 10. The RDS step on path **IIa\_cis\_L2** is similar to path **Ia\_cis\_L2**, but the free energy barrier of **TS3\_IIa\_cis\_L2** is only  $30.4 \text{ kcal}\cdot\text{mol}^{-1}$ , about  $10.4 \text{ kcal}\cdot\text{mol}^{-1}$  lower than that of **TS3\_Ia\_cis\_L2** ( $40.8 \text{ kcal}\cdot\text{mol}^{-1}$ , Figure S10). Meanwhile, the free energy barrier of the RDS transition state on path **IIa\_trans\_L2** (**TS2\_IIa\_trans\_L2**) is only  $31.2 \text{ kcal}\cdot\text{mol}^{-1}$ , also lower than that of **TS3\_Ia\_trans\_L2** ( $41.9 \text{ kcal}\cdot\text{mol}^{-1}$ , Figure S10). Clearly, when the monodentate phosphine ligand **L2** is employed, the optimal pathway is path **II** rather than path **I**.

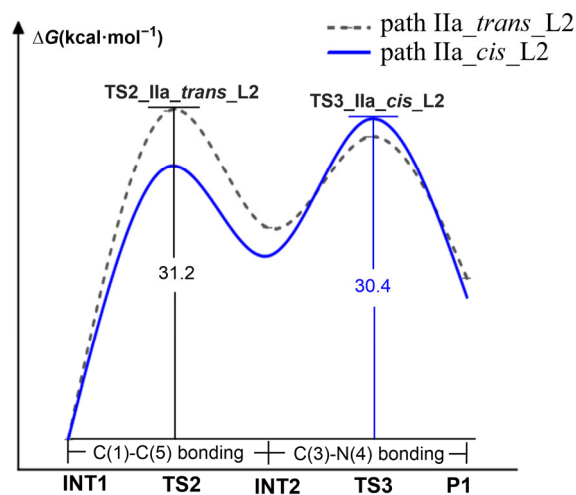


**Figure 10.** Potential free energy surfaces (PESs) for paths **IIa\_cis\_L2** (blue) and **IIa\_trans\_L2** (black dotted).

To confirm this inference, we continued to compute paths **I** and **II** assisted by the bidentate ligand **L3** and monodentate ligand **L4** (denoted paths **Ia\_cis\_L3**, **Ia\_trans\_L3**, **IIa\_cis\_L3**, **IIa\_trans\_L3**, **Ia\_cis\_L4**, **Ia\_trans\_L4**, **IIa\_cis\_L4** and **IIa\_trans\_L4**, respectively), with their potential free energy profiles presented in Figures S11 and S12. Indeed, the dominant pathway for the bidentate ligand **L3**-assisted one is path **I** (Figure S11), while the optimal pathway for the monodentate ligand **L4**-assisted reaction corresponds to path **II** (Figure S12). The **L3**-assisted RDS free energy barriers on path **I** (**TS2\_Ia\_cis\_L3** and **TS2\_Ia\_trans\_L3**) are  $26.7$  and  $28.3 \text{ kcal}\cdot\text{mol}^{-1}$ , respectively, in good accordance with the major formation of **P1\_cis** in experiment (Scheme 1). The **L4**-assisted free energy barriers of RDS transition states on path **II** (**TS3\_IIa\_cis\_L4** and **TS2\_IIa\_trans\_L4**) are  $30.2$  and

31.8 kcal·mol<sup>-1</sup>, respectively, also being consistent with the advantageous generation of **P1<sub>cis</sub>** over **P1<sub>trans</sub>**. Thus, it is believed the different coordination modes of monodentate and bidentate phosphine ligands can lead to alteration of the dominant pathway here.

This can also be well seen from the optimized geometries of some key transition states (Figure 11). For the bidentate ligand **L1**- and **L3**-assisted transition states, the nickel center coordinates with two P and two C atoms in them, so there are no more coordinate for surrounding hetero-atoms such as O or N atoms. Thus, the smaller steric hindrance between the phosphine ligand **L1/L3** and the rest of the molecule in the RDS transition states (**TS2\_Ia<sub>cis</sub>\_L1/L3** and **TS2\_Ia<sub>trans</sub>\_L1/L3**) on path **I** make it more feasible than path **II**. Nevertheless, in the monodentate ligand **L2**- and **L4**-assisted transition states, the nickel center coordinates with only one P and two C atoms, so it will coordinate extra with the O atom in the -Ts group or with the N atom in the *N*-tosylbenzaldimine fragment, resulting in more stable RDS transition states (**TS3\_Ila<sub>cis</sub>\_L2/L4** and **TS2\_Ila<sub>trans</sub>\_L2/L4**) on path **II** and making path **II** more preferred than path **I** in energy. Due to a significant reduction in relative energies caused by strong Ni–N or Ni–O coordination in **TS2\_Ila<sub>cis</sub>\_L2/L4** (Figure 11a), **TS3\_Ila<sub>cis</sub>\_L2/L4** becomes higher and the C(3)–N(4) bonding process acts as the RDS step on path **Ila**, as shown in Figure 10 and Figure S12b. NCI analysis results show more pronounced noncovalent interactions in **TS2\_Ila<sub>cis</sub>\_L2/L4** than in **TS3\_Ila<sub>cis</sub>\_L2/L4** accordingly, reflects well the different coordination modes of monodentate ligand **L2/L4** from bidentate ligand **L1/L3** to the nickel center result in different stabilities (Figure 11b). It also demonstrates that the electronic effects play a dominant role in controlling the rates and selectivities of the reaction.

As summarized in Table 2, the activation free energy barriers of **L1**–**L4**-assisted RDS transition states on their optimal pathway are completely consistent with the corresponding experimental trend in yield, and there is a good negative correlation between the RDS free energy barriers and the yields (Figure 12). Namely, the higher the RDS free energy barrier, the lower the yield of **P1**. What is more, the computationally predicted diastereoselectivity ratios (*dr*<sup>calc.</sup>) for **P1<sub>cis</sub>**:**P1<sub>trans</sub>** are in good agreement with experimentally detected *dr* values (*dr*<sup>Expt.</sup>), no matter the bidentate ligand **L1/L3** or the monodentate ligand **L2/L4** used. For example, the **L2**-assisted generation rate of **P1<sub>cis</sub>**, which transferred from the free energy barriers of the corresponding RDS transition state, is 3.8 times faster than that of **P1<sub>trans</sub>**, in perfect agreement with an experimental ratio of **P1<sub>cis</sub>**:**P1<sub>trans</sub>** = 3.3:1. To sum up, only product **P1<sub>cis</sub>** can be observed experimentally, no matter whether a bidentate phosphine ligand or a monodentate one is employed. The yields and selectivities predicted by theory have reproduced corresponding experimental results well, and showed the reliability of the computational predictions presented in this work.

**Table 2.** Free energy barriers ( $\Delta\Delta G$ , in kcal·mol<sup>-1</sup>) of RDS transition states ( $TS_{RDS}$ ) located on paths **Ia<sub>cis</sub>/trans<sub>L</sub>** and **Ila<sub>cis</sub>/trans<sub>L</sub>**, as well as the rate constants (*k*, L·mol<sup>-1</sup>·s<sup>-1</sup> or s<sup>-1</sup>), reaction half-lives (*t*<sub>1/2</sub>, h) and corresponding experimental reaction time, yield and *dr* ratios.

Ligand	$TS_{RDS}$	$\Delta\Delta G$	<i>k</i>	<i>t</i> <sub>1/2</sub> (h)	<i>t</i> <sup>Expt.</sup> (h)	Yield (%)	<i>dr</i> <sup>Calc.</sup>	<i>dr</i> <sup>Expt.</sup>
<b>L1</b> : dmpe	TS2_Ia <sub>cis</sub> _L1	25.1	$4.969 \times 10^{-6}$	$5.590 \times 10^1$	5 h	>99	19.9:1	>99:1
	TS2_Ia <sub>trans</sub> _L1	26.9	$2.500 \times 10^{-7}$	$1.111 \times 10^3$				
<b>L2</b> : PMe <sub>2</sub> Ph	TS3_Ila <sub>cis</sub> _L2	30.4	$7.474 \times 10^{-10}$	$2.576 \times 10^5$		47	3.8:1	3.3:1
	TS2_Ila <sub>trans</sub> _L2	31.2	$1.979 \times 10^{-10}$	$1.403 \times 10^6$				
<b>L3</b> : dppe	TS2_Ia <sub>cis</sub> _L3	26.7	$3.485 \times 10^{-7}$	$7.970 \times 10^2$		73	14.3:1	5.2:1
	TS2_Ia <sub>trans</sub> _L3	28.3	$2.445 \times 10^{-8}$	$1.136 \times 10^4$				
<b>L4</b> : PMe <sub>3</sub>	TS3_Ila <sub>cis</sub> _L4	30.2	$1.042 \times 10^{-9}$	$1.848 \times 10^5$		62	14.3:1	6.0:1
	TS2_Ila <sub>trans</sub> _L4	31.8	$7.307 \times 10^{-11}$	$3.802 \times 10^6$				

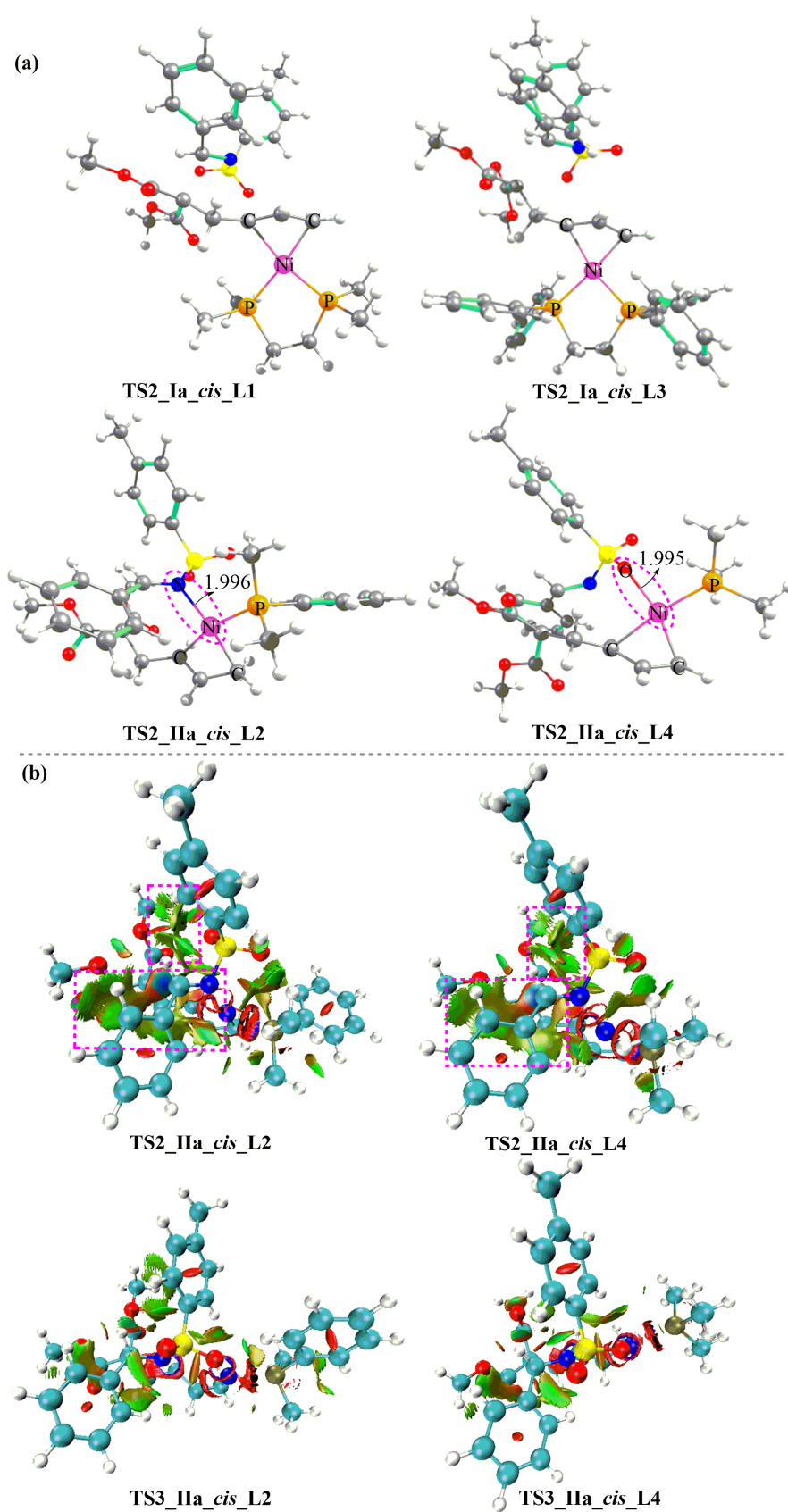


**Figure 11.** (a) Optimized geometries (with bond length in Å) for transition states TS2\_Ia\_cis\_L1/L3 and TS2\_IIa\_cis\_L2/L4, (b) NCI analysis results for transition states TS2\_IIa\_cis\_L2/L4 and TS3\_IIa\_cis\_L2/L4.

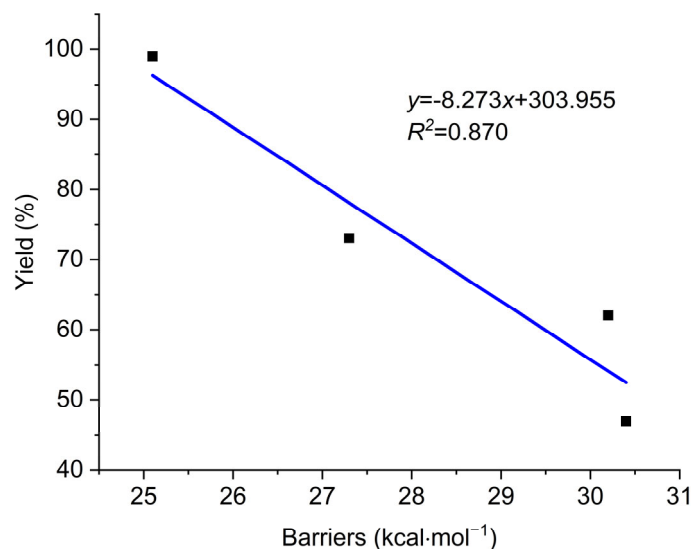


**Figure 12.** Correlations between RDS transition state barriers ( $\Delta\Delta G$ , in kcal·mol<sup>-1</sup>) and experimentally detected yield (%) of **P1\_cis**.

### 3. Computational Methods

All stationary points along the mechanistic profiles were initially optimized, with their identities verified and relative free energies determined employing the B3LYP density functional method [49,50] and the DGDZVP basis set [51,52] as implemented in the Gaussian 09 Program [53]. All models involved the full-sized systems for accurate representation of the real chemical transformations under investigation. Solvent effects were taken into account by optimizing all stationary points in acetonitrile (ACN,  $\epsilon = 37.5$ ) solvent, using the IDSCRF atomic radii [54] as implemented in the default self-consistent reaction field (SCRF) polarisable continuum model (PCM) [55], denoted IDSCRF(ACN)-B3LYP. All minima and transition states (TSs) are confirmed by frequency analysis. Intrinsic reaction coordinate (IRC) [56–58] calculations were carried out on selected transition states to confirm their correct connection to the two adjacent minima. All free energies reported throughout this work have been corrected to include translational entropy contributions in the condensed phase ( $S_{trans(l)}$ ) using the THERMO program [59], towards avoiding the pitfalls associated with default gas-phase determinations of  $S_{trans}$  originating from  $S_{trans(g)}$ . Natural bond orbital (NBO) analyses [36–38], as implemented in G09, were also performed on selected stationary points at the same level as geometry optimization, to investigate their electronic properties and bonding characteristics. NCI analyses [47] were carried out using Multiwfn [60], with the NCI isosurfaces (blue, interaction; green, weak interaction; brown, repulsion; red, strong repulsion) shown by employing Visual Molecular Dynamics (VMD) [61]. All 3D structures were drawn with CYLview [62].

To confirm the reliability of the methods used and discussed in the text, the dispersion-corrected DFT-D method [63,64] (denoted B3LYP-D3) and the most popular M06-2X functional [65] were chosen to optimize all stationary points involved on the dmpe (**L1**)-assisted paths **Ia\_cis** and **Ia\_trans**, with corresponding PESs shown in Figure S13 and the RDS transition state barriers summarized in Table S2 (the B3LYP results are also listed for the convenience of comparison). The RDS barriers on path **Ia\_cis** obtained by employing B3LYP, B3LYP-D3 and M06-2X functionals are predicted as 25.1, 8.7 and 14.3 kcal·mol<sup>-1</sup>, respectively, while their counterparts on path **Ia\_trans** are predicted as 26.9, 9.1 and 17.4 kcal·mol<sup>-1</sup>, respectively. Regardless of whether dispersion correction is included or not, all three functionals can predict the distereoselectivities correctly. However, the half-lives predicted by B3LYP-D3 and M06-2X methods deviate 7–11 orders of magnitude from corresponding reaction time, while the reaction half-lives predicted by the B3LYP method deviate only one order of magnitude. Namely, both B3LYP-D3 and M06-2X methods underestimated the RDS step's activation barriers, as people have found out in

their work [66–69]. This underestimation is probably caused by overestimation of weak interactions [68,70] between INT1\_I and R2 fragments. Thus, all free energies reported throughout this work are based on IDSCRF(ACN)–B3LYP/DGDZVP level’s computations and have been corrected to the experimental temperature of 303 K by using the THERMO program, unless noted elsewhere.

#### 4. Conclusions

Based on comprehensive density functional theory (DFT) studies on both bidentate (L1/L3)- and monodentate phosphine ligands (L2/L4)-assisted nickel-initiated [3+2] cycloaddition between vinylcyclopropanes (VCP) and *N*-tosylbenzaldimine, the following conclusions can be drawn: (1) The VCP substrate (R1) prefers to open its three-numbered ring through C(1)–C(3) bond cleavage along path I or II and converts to intermediate INT1\_I/INT1\_II smoothly. In the bidentate (L1, L3)-assisted cases, *C,C\_anti* path I is verified to be the most accessible one in generating the [3+2] cycloaddition products from the ring-opened intermediate INT1\_I, for it is more advantageous in avoiding possible spatial hindrance. *C,C\_syn* path II become more feasible in generating the [3+2] cycloaddition products from the ring-opened intermediate INT1\_II in the monodentate (L2, L4)-assisted cases, because extra Ni–O or Ni–N coordination can effectively reduce the activation barriers of corresponding RDS transition states. (2) The formation of C–C and C–N bonds between *N*-tosylbenzaldimine and the ring-opened intermediate (INT1\_I or INT1\_II) through [3+2] cycloaddition is found to be stepwise, with the former acting as the rate-determining step (RDS) in most cases (except for paths IIa\_cis\_L2 and IIa\_cis\_L4, in which the C–N bonding process acts as the RDS step due to strong Ni–N and Ni–O coordination in corresponding C–C bonding transition states). Computed free energy barriers of RDS transition states on L1–L4-assisted optimal path I or II transfer to good predictions for reaction half-lives and rate contents, and provide reasonable explanations for the diastereoselectivities detected in experiments. (3) Noncovalent interaction (NCI) analyses of key stationary points suggest the rate of this reaction is influenced by both electronic effects and steric hindrance, with the diastereoselectivity being mainly controlled by electronic effects. These results not only shed light on the mechanism of the nickel-initiated [3+2] cycloaddition between VCP and imines, but also provide new insights into the ligand role and selectivity-controlling mode of similar transition metal-catalyzed cycloadditions assisted by phosphine ligands.

**Supplementary Materials:** The following supporting information can be downloaded at: <https://www.mdpi.com/article/10.3390/catal14010082/s1>, Figure S1: PESs for paths I–V, Figure S2: The expected structure of complex COM1\_V, Figure S3: Optimized geometries of some stationary points located on paths I–V, Figure S4: QTAIM analysis results for some stationary points located on paths I–V, Figure S5: Key geometrical parameters in R1 and INT1\_III, Figures S6–S8: PESs for paths IIIb\_cis, Ib\_cis, IIB\_cis, IIIa\_cis, IIa\_cis and IIa\_trans, Figure S9: NCI analysis results for TS2\_Ia\_cis, TS2\_Ia\_trans, TS3\_Ia\_cis and TS3\_Ia\_trans, Figures S10–S12: PESs for paths Ia\_cis\_L2, Ia\_trans\_L2, Ia\_cis\_L3, Ia\_trans\_L3, IIa\_cis\_L3, IIa\_trans\_L3, Ia\_cis\_L4, Ia\_trans\_L4, IIa\_cis\_L4 and IIa\_trans\_L4, Figure S13: PESs for paths Ia\_cis and Ia\_trans obtained by employing B3LYP, B3LYP–D3 and M06–2X methods, Tables S1 and S2: Free energy barriers and corresponding kinetic data for RDS transition states, Tables S3–S8: Optimized Cartesian coordinates for stationary points, Tables S9–S14: The first three vibrational frequencies for stationary points, Tables S15–S20: Energetic results for stationary points obtained at different computational levels.

**Author Contributions:** Data curation, W.M., S.X. and X.T.; Funding acquisition, W.M. and G.M.; Conceptualization and supervision, W.M.; Project administration, W.M. and G.L.; Visualization, W.M., L.Z. and X.T.; Writing—original draft, W.M. and S.X.; Writing—review and editing, W.M., L.Z., L.D., G.M. and G.L. All authors have read and agreed to the published version of the manuscript.

**Funding:** This research was funded by the National Natural Science Foundation of China (grant number 22363012, 21763033), Top Young Talents of Yunnan Ten Thousand People Plan, Yunnan Fundamental Research Projects (grant number 202301AT070081) and the PhD Scientific Research Start-up Projects of Yunnan Normal University.

**Data Availability Statement:** The original data are included in the article and Supplementary Materials. Further inquiries can be directly addressed to the corresponding author.

**Acknowledgments:** The authors acknowledge Jingxuan Zhang and Tao Yu (in Faculty of Chemistry and Chemical Engineering, Yunnan Normal University) for helpful discussion during the organization, writing and revision of this manuscript.

**Conflicts of Interest:** The authors declare no conflicts of interest.

## References

1. Landrain, Y.; Evano, G. Synthesis of Tetrahydrofurans and Pyrrolidines by Copper Catalyzed Oxy/Aminoarylation of Alkenes. *Org. Lett.* **2023**, *25*, 3898–3903. [[CrossRef](#)] [[PubMed](#)]
2. Mailyan, A.K.; Eickhoff, J.A.; Minakova, A.S.; Gu, Z.; Lu, P.; Zakarian, A. Cutting-Edge and Time-Honored Strategies for Stereoselective Construction of C–N Bonds in Total Synthesis. *Chem. Rev.* **2016**, *116*, 4441–4557. [[CrossRef](#)] [[PubMed](#)]
3. Nakagawa, H.; Fuwa, H. Au-Catalyzed Stereodivergent Synthesis of 2, 5-Disubstituted Pyrrolidines: Total Synthesis of (+)-Monomorine I and (+)-Indolizidine 195B. *Chem. Commun.* **2023**, *59*, 10121–10124. [[CrossRef](#)] [[PubMed](#)]
4. Zhang, F.; Dai, X.; Dai, L.; Zheng, W.; Chan, W.L.; Tang, X.; Zhang, X.; Lu, Y. Phosphine-Catalyzed Enantioselective (3+2) Annulation of Vinylcyclopropanes with Imines for the Synthesis of Chiral Pyrrolidines. *Angew. Chem. Int. Ed.* **2022**, *61*, e202203212. [[CrossRef](#)] [[PubMed](#)]
5. Ma, X.; Hazelden, I.R.; Langer, T.; Munday, R.H.; Bower, J.F. Enantioselective Aza-Heck Cyclizations of *N*-(Tosyloxy) Carbamates: Synthesis of Pyrrolidines and Piperidines. *J. Am. Chem. Soc.* **2019**, *141*, 3356–3360. [[CrossRef](#)] [[PubMed](#)]
6. Hashimoto, T.; Maruoka, K. Recent Advances of Catalytic Asymmetric 1,3-Dipolar Cycloadditions. *Chem. Rev.* **2015**, *115*, 5366–5412. [[CrossRef](#)]
7. Hazelden, I.R.; Carmona, R.C.; Langer, T.; Pringle, P.G.; Bower, J.F. Pyrrolidines and Piperidines by Ligand-Enabled Aza-Heck Cyclizations and Cascades of *N*-(Pentafluorobenzoyloxy)Carbamates. *Angew. Chem. Int. Ed.* **2018**, *57*, 5124–5128. [[CrossRef](#)]
8. Lee, S.; Lei, H.; Rovis, T. A Rh(III)-Catalyzed Formal [4+1] Approach to Pyrrolidines from Unactivated Terminal Alkenes and Nitrene Sources. *J. Am. Chem. Soc.* **2019**, *141*, 12536–12540. [[CrossRef](#)]
9. Yamazaki, K.; Gabriel, P.; Carmine, G.D.; Pedroni, J.; Farizyan, M.; Hamlin, T.A.; Dixon, D.J. General Pyrrolidine Synthesis via Iridium-Catalyzed Reductive Azomethine Ylide Generation from Tertiary Amides and Lactams. *ACS Catal.* **2021**, *11*, 7489–7497. [[CrossRef](#)]
10. He, F.S.; Li, C.S.; Deng, H.; Zheng, X.; Yang, Z.T.; Deng, W.P. The Facile and Stereoselective Synthesis of Pyrrolidine  $\beta$ -Amino Acids via Copper(i)-Catalyzed Asymmetric 1,3-Dipolar Cycloaddition. *Org. Chem. Front.* **2017**, *4*, 52–56. [[CrossRef](#)]
11. Lin, T.Y.; Zhu, C.Z.; Zhang, P.; Wang, Y.; Wu, H.H.; Feng, J.J.; Zhang, J. Regiodivergent Intermolecular [3+2] Cycloadditions of Vinyl Aziridines and Allenes: Stereospecific Synthesis of Chiral Pyrrolidines. *Angew. Chem. Int. Ed.* **2016**, *55*, 10844–10848. [[CrossRef](#)] [[PubMed](#)]
12. Chen, H.; Zhong, W.; Liu, S.; Zou, T.; Zhang, K.; Gong, C.; Guo, W.; Kong, F.; Nie, L.; Hu, S.; et al. Highly Stereodivergent Synthesis of Chiral C4-Ester-Quaternary Pyrrolidines: A Strategy for the Total Synthesis of Spirotryprostatin A. *Org. Lett.* **2023**, *25*, 3391–3396. [[CrossRef](#)] [[PubMed](#)]
13. Das, D.; Mohapatra, S.S.; Roy, S. Recent Advances in Heterobimetallic Catalysis across a “Transition Metal–Tin” Motif. *Chem. Soc. Rev.* **2015**, *44*, 3666–3690. [[CrossRef](#)] [[PubMed](#)]
14. Genet, J.P.; Ayad, T.; Ratovelomanana-Vidal, V. Electron-Deficient Diphosphines: The Impact of DIFLUORPHOS in Asymmetric Catalysis. *Chem. Rev.* **2014**, *114*, 2824–2880. [[CrossRef](#)]
15. Zhang, D.; Wang, Q. Palladium Catalyzed Asymmetric Suzuki–Miyaura Coupling Reactions to Axially Chiral Biaryl Compounds: Chiral Ligands And Recent Advances. *Coordin. Chem. Rev.* **2015**, *286*, 1–16. [[CrossRef](#)]
16. Schmitz, C.; Holthausen, K.; Leitner, W.; Franciò, G. Highly Regio- and Enantioselective Hydroformylation of Vinyl Esters Using Bidentate Phosphine,P-Chiral Phosphorodiamidite Ligands. *ACS Catal.* **2016**, *6*, 1584–1589. [[CrossRef](#)]
17. Souillart, L.; Cramer, N. Highly Enantioselective Rhodium(I)-Catalyzed Carbonyl Carboacylations Initiated by C–C Bond Activation. *Angew. Chem. Int. Ed.* **2014**, *53*, 9640–9644. [[CrossRef](#)]
18. Noucti, N.N.; Alexanian, E.J. Stereoselective Nickel-Catalyzed [2+2+2] Cycloadditions and Alkenylative Cyclizations of Ene-Allenenes and Alkenes. *Angew. Chem. Int. Ed.* **2013**, *52*, 8424–8427. [[CrossRef](#)]
19. Ding, Z.; Wang, Y.; Liu, W.; Chen, Y.; Kong, W. Diastereo- and Enantioselective Construction of Spirocycles by Nickel-Catalyzed Cascade Borrowing Hydrogen Cyclization. *J. Am. Chem. Soc.* **2021**, *143*, 53–59. [[CrossRef](#)]
20. Tombe, R.; Kurahashi, T.; Matsubara, S. Nickel-Catalyzed Cycloaddition of Vinylcyclopropanes to Imines. *Org. Lett.* **2013**, *15*, 1791–1793. [[CrossRef](#)]
21. Peng, Q.; Paton, R.S. Catalytic Control in Cyclizations: From Computational Mechanistic Understanding to Selectivity Prediction. *Acc. Chem. Res.* **2016**, *49*, 1042–1051. [[CrossRef](#)] [[PubMed](#)]
22. Wang, Q.; Huang, F.; Jiang, L.; Sun, C.; Liu, J.; Chen, D. A Mechanistic Insight into the Ligand-Controlled Asymmetric Arylation of Aliphatic  $\alpha$ -Amino Anion Equivalents: Origin of Regioand Enantioselectivities. *Inorg. Chem.* **2017**, *56*, 5984–5992. [[CrossRef](#)] [[PubMed](#)]

23. Dub, P.A.; Gordon, J.C. Metal–Ligand Bifunctional Catalysis: The “Accepted” Mechanism, the Issue of Concertedness, and the Function of the Ligand in Catalytic Cycles Involving Hydrogen Atoms. *ACS Catal.* **2017**, *7*, 6635–6655. [[CrossRef](#)]
24. Jover, J.; Maseras, F. Mechanistic Investigation of Iridium–Catalyzed C–H Borylation of Methyl Benzoate: Ligand Effects in Regioselectivity and Activity. *Organometallics* **2016**, *35*, 3221–3226. [[CrossRef](#)]
25. Bhunya, S.; Roy, L.; Paul, A. Mechanistic Details of Ru–Bispyridylborate Complex Catalyzed Dehydrogenation of Ammonia–Borane: The Role of Pendant Boron Ligand in Catalysis. *ACS Catal.* **2016**, *6*, 4068–4080. [[CrossRef](#)]
26. Parsons, A.T.; Champbell, M.J.; Johnson, J.S. Diastereoselective Synthesis of Tetrahydrofurans via Palladium(0)–Catalyzed [3+ 2] Cycloaddition of Vinylcyclopropanes and Aldehydes. *Org. Lett.* **2008**, *10*, 2541–2544. [[CrossRef](#)]
27. Novikov, R.A.; Tarasova, A.V.; Korolev, V.A.; Shulishov, E.V.; Timofeev, V.P.; Tomilov, Y.V. Donor–Acceptor Cyclopropanes as 1,2–Dipoles in GaCl<sub>3</sub>–Mediated [4 + 2]–Annulation with Alkenes–Easy Access to Tetralin Skeleton. *J. Org. Chem.* **2015**, *80*, 8225–8235. [[CrossRef](#)]
28. Rivero, A.R.; Fernández, I.; de Arellano, C.R.; Sierra, M.A. Synthesis of Oxaspiranic Compounds Through [3+2] Annulation of Cyclopropanones and Donor–Acceptor Cyclopropanes. *J. Org. Chem.* **2015**, *80*, 1207–1213. [[CrossRef](#)]
29. Chen, Z.; Tian, Z.; Zhang, J.; Ma, J.; Zhang, J. C–O Versus C–C Bond Cleavage: Selectivity Control in Lewis Acid Catalyzed Chemodivergent Cycloadditions of Aryl Oxiranyldicarboxylates with Aldehydes, and Theoretical Rationalizations of Reaction Pathways. *Chem. Eur. J.* **2012**, *18*, 8591–8595. [[CrossRef](#)]
30. Kaicharla, T.; Roy, T.; Thangaraj, M.; Gonnade, R.G.; Biju, A.T. Lewis Acid Catalyzed Selective Reactions of Donor–Acceptor Cyclopropanes with 2–Naphthols. *Angew. Chem. Int. Ed.* **2016**, *55*, 10061–10064. [[CrossRef](#)]
31. Borisov, D.D.; Novikov, R.A.; Tomilov, Y.V. GaCl<sub>3</sub>–Mediated Reactions of Donor–Acceptor Cyclopropanes with Aromatic Aldehydes. *Angew. Chem. Int. Ed.* **2016**, *55*, 12233–12237. [[CrossRef](#)] [[PubMed](#)]
32. Grover, H.K.; Emmett, M.R.; Kerr, M.A. Carbocycles from Donor–Acceptor Cyclopropanes. *Org. Biomol. Chem.* **2015**, *13*, 655–671. [[CrossRef](#)] [[PubMed](#)]
33. Liu, Z.S.; Li, W.K.; Kang, T.R.; He, L.; Liu, Q.Z. Palladium–Catalyzed Asymmetric Cycloadditions of Vinylcyclopropanes and in Situ Formed Unsaturated Imines: Construction of Structurally and Optically Enriched Spiroindolenines. *Org. Lett.* **2015**, *17*, 150–153. [[CrossRef](#)] [[PubMed](#)]
34. Garve, L.K.B.; Werz, D.B. Pd–Catalyzed Three–Component Coupling of Terminal Alkynes, Arynes, and Vinyl Cyclopropane Dicarboxylate. *Org. Lett.* **2015**, *17*, 596–599. [[CrossRef](#)]
35. Song, C.; Dang, Y.; Tao, Y.; Wang, Z.X. DFT Mechanistic Study of Functionalizations of  $\omega$ –Ene–Cyclopropanes and Alkylidenecyclopropanes via Allylic C–H and C–C Bond Cleavage Facilitated by a Zirconocene Complex. *Organometallics* **2015**, *34*, 5233–5244. [[CrossRef](#)]
36. Reed, A.E.; Curtiss, L.A.; Weinhold, F. Intermolecular Interactions from a Natural Bond Orbital, Donor–Acceptor Viewpoint. *Chem. Rev.* **1988**, *88*, 899–926. [[CrossRef](#)]
37. Reed, A.E.; Weinstock, R.B.; Weinhold, F. Natural Population Analysis. *J. Chem. Phys.* **1985**, *83*, 735–746. [[CrossRef](#)]
38. Carpenter, J.E.; Weinhold, F. Analysis of the Geometry of the Hydroxymethyl Radical by the “Different Hybrids for Different Spins” Natural Bond Orbital Procedure. *J. Mol. Struct.* **1988**, *169*, 41–62. [[CrossRef](#)]
39. Brown, C.; Lita, A.; Tao, Y.; Peek, N.; Crosswhite, M.; Mileham, M.; Krzystek, J.; Achey, R.; Fu, R.; Bindra, J.K.; et al. Mechanism of Initiation in the Phillips Ethylene Polymerization Catalyst: Ethylene Activation by Cr(II) and the Structure of the Resulting Active Site. *ACS Catal.* **2017**, *7*, 7442–7455. [[CrossRef](#)]
40. Bader, R.F.W. A Quantum Theory of Molecular Structure and Its Applications. *Chem. Rev.* **1991**, *91*, 893–928. [[CrossRef](#)]
41. Bader, R.F.W. *Atoms in Molecules: A Quantum Theory*; Clarendon Press: Oxford, UK, 1990.
42. Maji, R.; Champagne, P.A.; Houk, K.N.; Wheeler, S.E. Activation Mode and Origin of Selectivity in Chiral Phosphoric Acid Catalyzed Oxacycle Formation by Intramolecular Oxetane Desymmetrizations. *ACS Catal.* **2017**, *7*, 7332–7339. [[CrossRef](#)]
43. Duan, A.; Yu, P.; Liu, F.; Qiu, H.; Gu, F.L.; Doyle, M.P.; Houk, K.N. Diazo Esters as Dienophiles in Intramolecular (4+2) Cycloadditions: Computational Explorations of Mechanism. *J. Am. Chem. Soc.* **2017**, *139*, 2766–2770. [[CrossRef](#)] [[PubMed](#)]
44. Bickelhaupt, F.M.; Houk, K.N. Analyzing Reaction Rates with the Distortion/Interaction–Activation Strain Model. *Angew. Chem. Int. Ed.* **2017**, *56*, 10070–10086. [[CrossRef](#)] [[PubMed](#)]
45. Xiong, Y.; Du, Z.; Chen, H.; Yang, Z.; Tan, Q.; Zhang, C.; Zhu, L.; Lan, Y.; Zhang, M. Well–Designed Phosphine–Urea Ligand for Highly Diastereo–and Enantioselective 1,3–Dipolar Cycloaddition of Methacrylonitrile: A Combined Experimental and Theoretical Study. *J. Am. Chem. Soc.* **2019**, *141*, 961–971. [[CrossRef](#)]
46. Lewars, E.G. *Computational Chemistry–Introduction to the Theory and Applications of Molecular and Quantum Mechanics*, 2nd ed.; Springer: Dordrecht, The Netherlands, 2011; pp. 9–40.
47. Johnson, E.R.; Keinan, S.; Mori–Sánchez, P.; Contreras–García, J.; Cohen, A.J.; Yang, W. Revealing Noncovalent Interactions. *J. Am. Chem. Soc.* **2010**, *132*, 6498–6506. [[CrossRef](#)]
48. Dieskau, A.P.; Holzwarth, M.S.; Plietker, B. Fe–Catalyzed Allylic C–C–Bond Activation: Vinylcyclopropanes as Versatile a<sub>1</sub>,a<sub>3</sub>,d<sub>5</sub>–Synthons in Traceless Allylic Substitutions and [3+2]–Cycloadditions. *J. Am. Chem. Soc.* **2012**, *134*, 5048–5051. [[CrossRef](#)]
49. Lee, C.; Yang, W.; Parr, R.G. Development of the Colle–Salvetti Correlation–Energy Formula into a Functional of the Electron Density. *Phys. Rev. B* **1988**, *37*, 785–789. [[CrossRef](#)]
50. Becke, A.D. Perspective on “Density Functional Thermochemistry. III. The Role of Exact Exchange”. *J. Chem. Phys.* **1993**, *98*, 5648–5652. [[CrossRef](#)]

51. Godbout, N.; Salahub, D.R.; Andzelm, J.; Wimmer, E. Optimization of Gaussian-type Basis Sets for Local Spin Density Functional Calculations. Part I. Boron through Neon, Optimization Technique and Validation. *Can. J. Chem.* **1992**, *70*, 560–571. [[CrossRef](#)]
52. Sosa, C.; Andzelm, J.; Elkin, B.C.; Wimmer, E.; Dobbs, K.D.; Dixon, D.A. A Local Density Functional Study of the Structure and Vibrational Frequencies of Molecular Transition–Metal Compounds. *J. Phys. Chem.* **1992**, *96*, 6630–6636. [[CrossRef](#)]
53. Frisch, M.J.; Trucks, G.W.; Schlegel, H.B.; Scuseria, G.E.; Robb, M.A.; Cheeseman, J.R.; Scalmani, G.; Barone, V.; Mennucci, B.; Petersson, G.A.; et al. *Gaussian 09, Revision D.01*; Gaussian, Inc.: Wallingford, CT, USA, 2013.
54. Tao, J.Y.; Mu, W.H.; Chass, G.A.; Tang, T.H.; Fang, D.C. Balancing the Atomic Waistline: Isodensity–Based SCRF Radii for Main–Group Elements and Transition Metals. *Int. J. Quantum Chem.* **2013**, *113*, 975–984. [[CrossRef](#)]
55. Miertus, S.; Scrocco, E.; Tomasi, J. Electrostatic Interaction of a Solute with a Continuum. A Direct Utilizaion of AB Initio Molecular Potentials for the Prevision of Solvent Effects. *Chem. Phys.* **1981**, *55*, 117–129. [[CrossRef](#)]
56. Gonzalez, C.; Schlegel, H.B. An Improved Algorithm for Reaction Path Following. *J. Chem. Phys.* **1989**, *90*, 2154–2161. [[CrossRef](#)]
57. Gonzalez, C.; Schlegel, H.B. Reaction Path Following in Mass–Weighted Internal Coordinates. *J. Phys. Chem.* **1990**, *94*, 5523–5527. [[CrossRef](#)]
58. Fukui, K. The Path of Chemical Reactions–the IRC Approach. *Acc. Chem. Res.* **1981**, *14*, 363–368. [[CrossRef](#)]
59. Fang, D.C. *THERMO*; Beijing Normal University: Beijing, China, 2013.
60. Lu, T.; Chen, F.W. Multiwfn: A Multifunctional Wavefunction Analyzer. *J. Comput. Chem.* **2012**, *33*, 580–592. [[CrossRef](#)] [[PubMed](#)]
61. Humphrey, W.; Dalke, A.; Schulten, K. VMD: Visual Molecular Dynamics. *J. Mol. Graph.* **1996**, *14*, 33–38. [[CrossRef](#)] [[PubMed](#)]
62. Legault, C.Y. *CYLVIEW, 1.0b*; Université de Sherbrooke: Sherbrooke, QC, Canada, 2009.
63. Grimme, S. Semiempirical GGA–Type Density Functional Constructed with a Long–Range Dispersion Correction. *J. Comput. Chem.* **2006**, *27*, 1787–1799. [[CrossRef](#)]
64. Grimme, S.; Antony, J.; Ehrlich, S.; Krieg, H. A Consistent and Accurate Ab Initio Parametrization of Density Functional Dispersion Correction (DFT–D) for the 94 Elements H–Pu. *J. Chem. Phys.* **2010**, *132*, 154104–154119. [[CrossRef](#)]
65. Zhao, Y.; Truhlar, D.G. Comparative DFT Study of Van Der Waals Complexes: Rare–Gas Dimers, Alkaline–Earth Dimers, Zinc Dimer, and Zinc–Rare–Gas Dimers. *J. Phys. Chem.* **2006**, *110*, 5121–5129. [[CrossRef](#)]
66. Li, Y.; Fang, D.C. DFT Calculations On Kinetic Data For Some [4+2] Reactions in Solution. *Phys. Chem. Chem. Phys.* **2014**, *16*, 15224–15230. [[CrossRef](#)] [[PubMed](#)]
67. Mu, W.H.; Xia, S.Y.; Li, J.X.; Fang, D.C.; Wei, G.; Chass, G.A. Competing Mechanisms, Substituent Effect and Regioselectivities of Ni–Catalyzed [2+2+2] Cycloaddition between Carboryne and Alkynes: A DFT Study. *J. Org. Chem.* **2015**, *80*, 9108–9117. [[CrossRef](#)] [[PubMed](#)]
68. Ding, L.; Ishida, N.; Murakami, M.; Morokuma, K.  $sp^3$ – $sp^2$  vs  $sp^3$ – $sp^3$  C–C Site Selectivity in Rh–Catalyzed Ring Opening of Benzocyclobutenol: A DFT Study. *J. Am. Chem. Soc.* **2014**, *136*, 169–178. [[CrossRef](#)] [[PubMed](#)]
69. Chen, Y.M.; Chass, G.A.; Fang, D.C. Between a Reactant Rock and a Solvent Hard Place–Molecular Corrals Guide Aromatic Substitutions. *Phys. Chem. Chem. Phys.* **2014**, *16*, 1078–1083. [[CrossRef](#)]
70. Fang, D.; Chen, Y. Theoretical Studies on the Mechanism of Cycloaddition Reaction between 1,2,4,5–Tetrazine and Cycloolefines. *Acta Chim. Sin.* **2014**, *72*, 253–256. [[CrossRef](#)]

**Disclaimer/Publisher’s Note:** The statements, opinions and data contained in all publications are solely those of the individual author(s) and contributor(s) and not of MDPI and/or the editor(s). MDPI and/or the editor(s) disclaim responsibility for any injury to people or property resulting from any ideas, methods, instructions or products referred to in the content.